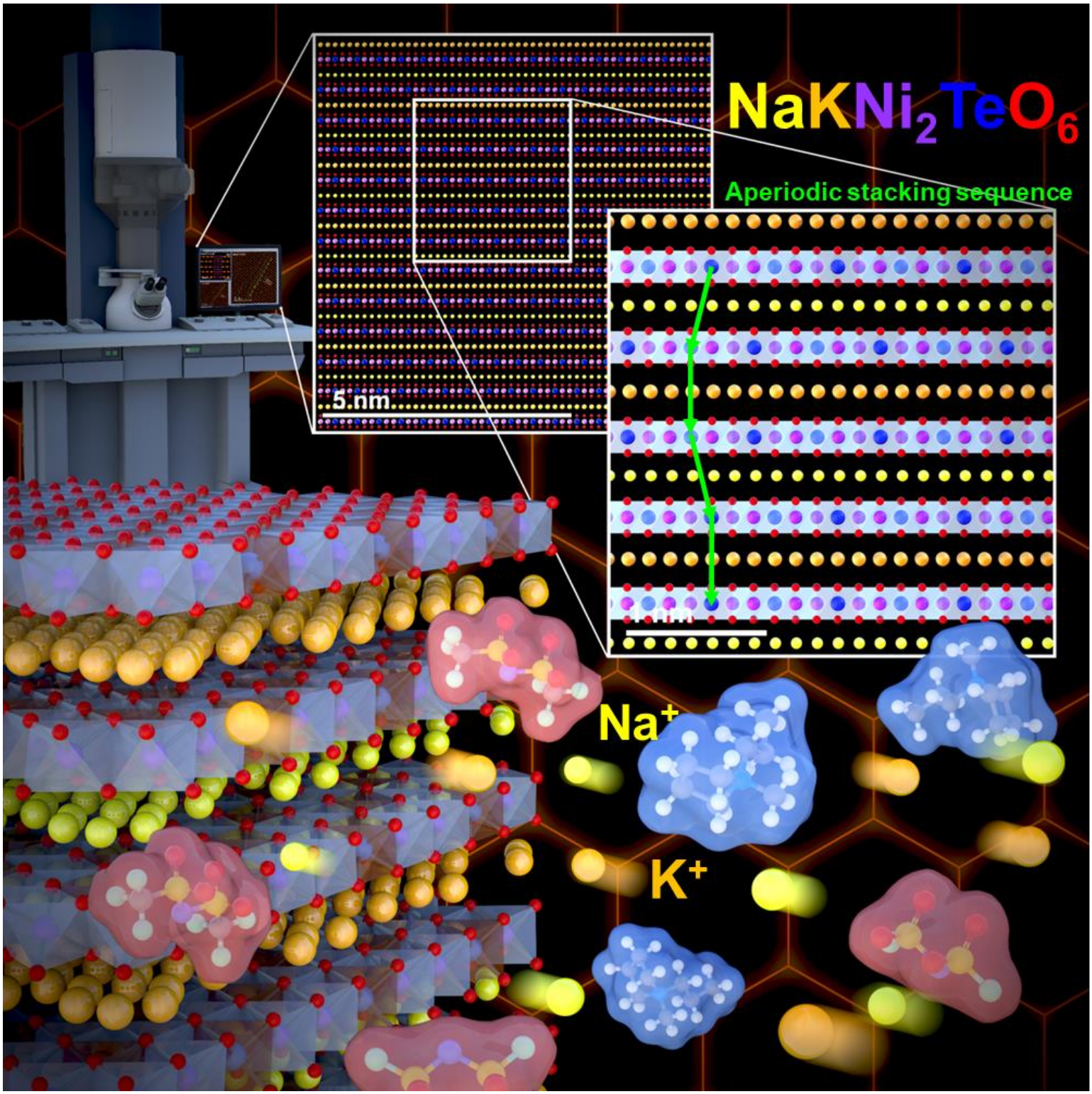

Stacking Disorders in Mixed-Alkali Honeycomb Layered Oxide $NaKNi_2TeO_6$ and Feasibility for Mixed-Cation Transport

Titus Masese[a,b], Yoshinobu Miyazaki[c], Josef Rizell[a,d], Godwill Mbiti Kanyolo[e], Chih-Yao Chen[b], Hiroki Ubukata[f], Keigo Kubota[b], Kartik Sau[g], Tamio Ikeshoji[g], Zhen-Dong Huang[h], Kazuki Yoshii[a], Teruo Takahashi[c], Miyu Ito[c], Hiroshi Senoh[a] , Jinkwang Hwang[i], Abbas Alshehabi[j], Kazuhiko Matsumoto[b,i], Toshiyuki Matsunaga[k], Kotaro Fujii[l], Masatomo Yashima[l], Masahiro Shikano[a], Cédric Tassel[f], Hiroshi Kageyama[f], Yoshiharu Uchimoto[k], Rika Hagiwara [b, i] & Tomohiro Saito[c]

[a] Research Institute of Electrochemical Energy, National Institute of Advanced Industrial Science and Technology (AIST), 1–8–31 Midorigaoka, Ikeda, Osaka 563–8577, JAPAN
Josef Rizell[a,d], Titus Masese[a,b], Kazuki Yoshii[b], Hiroshi Senoh[b]

[b] AIST-Kyoto University Chemical Energy Materials Open Innovation Laboratory (ChEM-OIL), Sakyo–ku, Kyoto 606–8501, JAPAN
Titus Masese[b,d], Chih-Yao Chen[d], Kazuhiko Matsumoto [d,i], Rika Hagiwara [d,i]

[c] Tsukuba Laboratory, Technical Solution Headquarters, Sumika Chemical Analysis Service (SCAS), Ltd.,Tsukuba, Ibaraki 300–3266, JAPAN
Yoshinobu Miyazaki[a], Teruo Takahashi[a], Miyu Ito[a], Tomohiro Saito[a]

[d] Department of Physics, Chalmers University of Technology, SE–412 96 Göteborg, SWEDEN.
Josef Rizell[a,d]

[e] Department of Engineering Science, The University of Electro–Communications, 1–5–1 Chofugaoka, Chofu, Tokyo 182–8585, JAPAN
Godwill Mbiti Kanyolo[e]

[f] Department of Energy and Hydrocarbon Chemistry, Graduate School of Engineering, Kyoto University, Nishikyo–ku, Kyoto 615–8510, JAPAN
Hiroki Ubukata[f], Cédric Tassel[f], Hiroshi Kageyama[f]

[g] Mathematics for Advanced Materials - Open Innovation Laboratory (MathAM-OIL), National Institute of Advanced Industrial Science and Technology (AIST), c/o Advanced Institute of Material Research (AIMR), Tohoku University, Sendai 980–8577, JAPAN
Kartik Sau[f], Tamio Ikeshoji[f]

[h] Key Laboratory for Organic Electronics and Information Displays and Institute of Advanced Materials (IAM), Nanjing University of Posts and Telecommunications (NUPT), Nanjing, 210023, CHINA
Zhen-Dong Huang[g]

[i] Graduate School of Energy Science, Kyoto University, Sakyo–ku, Kyoto 606–8501, JAPAN
Jinkwang Hwang[i], Kazuhiko Matsumoto [b,i], Rika Hagiwara [b,i]

[j] Department of Industrial Engineering, National Institute of Technology (KOSEN), Ibaraki College, 866 Nakane, Hitachinaka, Ibaraki 312–8508 JAPAN

Abbas Alshehabi

[k] Graduate School of Human and Environmental Studies, Kyoto University, Sakyo–ku, Kyoto 606–8501, JAPAN

Toshiyuki Matsunaga[j], Yoshiharu Uchimoto[j]

[l] Department of Chemistry, School of Science, Tokyo Institute of Technology, 2–12–1–W4–17 O–okayama, Meguro–ku, Tokyo, 152–8551, JAPAN

Kotaro Fujii[k], Masatomo Yashima[k]

*Correspondence and material requests should be addressed to: Titus Masese (Lead contact)

E-mail address: titus.masese@aist.go.jp

Phone: +81–72–751–9224; Fax: +81–72–751–9609

Abstract

In this study, we demonstrate the feasibility of using a combination of alkali atoms (Na and K) to develop a robust mixed-alkali honeycomb layered oxide: $NaKNi_2TeO_6$. Through a series of atomic-resolution transmission electron microscopy in multiple zone axes, we reveal for the first time the local atomic structural disorders characterised by aperiodic stackings and incoherency in the alternating arrangement of Na and K atoms. Our findings indicate great structural versatility that renders $NaKNi_2TeO_6$ an ideal platform for investigating other fascinating properties such as mixed ionic transport and intriguing electromagnetic and quantum phenomena amongst honeycomb layered oxides. Finally, we unveil the possibility of inducing mixed Na- and K-ion transport electrochemistry of $NaKNi_2TeO_6$ at high voltages (~ 4V), thus epitomising it as a competent cathode candidate for the emerging dendrite-free batteries based on NaK liquid metal alloy as anodes. The results not only betoken a new avenue for developing functional materials with fascinating crystal versatility, but also prefigure a new age of 'dendrite-free' energy storage system designs that rely on mixed-cation electrochemistry.

INTRODUCTION

Honeycomb layered oxides are a family of lamellar-structured nanomaterials characterised by alkali or coinage metal atoms interleaved between sheets of transition metal atoms aligned in a honeycomb formation. This emerging class has been gaining momentous interest as a result of a smörgåsbord of appealing properties innate to their structural framework. [1–10] The alkali- or coinage-metal atoms manifest weak interlayer bonds that engender an abundance of unoccupied sites that induce excellent ionic conductivities. This allows for facile reinsertion and extraction of alkali ions between the transition metal sheets, thus earmarking these materials as pedagogical exemplars of high-voltage cathodes for a novel class of rechargeable batteries. [1,2,11–17] Furthermore, the sandwiching of non-magnetic atoms between a hexagonal sublattice comprising magnetic atoms results in pseudo-two-dimensional magnetic structures that have the potential to achieve exotic magnetic states with varied applications in fields such as quantum computing and solid-state physics. [1,10]

Most honeycomb layered oxides encompass compositions; $A_2M_2DO_6$, $A_3M_2DO_6$ or A_4MDO_6 where A is an alkali- or coinage metal atom (A = Li, Na, K, Cu, Ag, …), M is a transition metal atom (M = Ni, Co, Mg, Zn, Mn, Fe, Cr, …) and D is a highly-valent ion like Te, Sb, Bi or W. [11] In these compositions, A atoms are sandwiched between slabs comprising M atoms surrounded by D atoms in a hexagonal formation. Depending on the atomic size of the A atom, the resulting lamellar structures manifest different sequential arrangements (hereupon referred to as stacking orders). Until now, only a handful of honeycomb layered oxides adopting T2-, O1-, O3- and P2-type (in Delmas' notation) stacking orders have been identified, whereby 'T', 'O' and 'P' denote the tetrahedral, octahedral or prismatic coordination of oxygen with the A atoms, whilst the ensuing digit corresponds to the number of repeating transition metal layers in the unit cell. [18] In order to further expand the scope of known honeycomb layered oxides and capitalise on their full potential, it is imperative to not only explore hitherto uncharted territories of their compositional space but also scrutinise their emergent stacking orders.

Amongst other classes of layered transition metal oxides, fascinating structures have been developed through the mixing of two different alkali species to formulate $A_xA'_yMO_2$ compositions. For instance, in the commonly studied $Li_xNa_yCoO_2$ layered cobaltate, the intermixing of similar amounts of Na and Li results in unique configurations of Na and Li within the different layers giving rise to versatile stacking structures ranging from OP4 to OPP9 stacking sequences. [19,20] This structural versatility facilitates the development of

manifold crystal structures with myriad potential to host exquisite functionalities. Materials such as $Li_{0.48}Na_{0.35}CoO_2$ have been found to exhibit a large thermoelectric power (thermopower) at room temperature, surpassing that of either of its parent materials, Na_yCoO_2 and Li_xCoO_2. [21] Furthermore, the unique OP4 stacking sequence has found great utility in battery application as it allows $Li_xNa_yCoO_2$ to be utilised as a precursor in ion-exchange synthesis to create a new polymorph electrode material $LiCoO_2$ with O4-stacking. [22,23]

Although the intermixing of alkali ions appears to be a judicious approach to the next level development of honeycomb layered oxides, as far as we can tell, only one report on a set of metastable antimonates $Li_{3-x}Na_xNi_2SbO_6$ has been published on the topic. [24] Thus, in an attempt to gain deeper insights, herein we investigate a novel composition of $Na_{2-x}K_xNi_2TeO_6$ honeycomb layered oxides. In this study, we utilise $Na_2Ni_2TeO_6$ and $K_2Ni_2TeO_6$ as the parent materials for the creation of a novel stable mixed alkali ion phase. The P2-type stacking (crystallising in the centrosymmetric $P6_3/mcm$ hexagonal space group) exhibited by both parent materials ($Na_2Ni_2TeO_6$ and $K_2Ni_2TeO_6$) is explicitly illustrated in **Figure 1a**, together with possible structural models for the resulting mixed compounds.

Furthermore, we unravel the structure of the new mixed alkali ion layered oxide $NaKNi_2TeO_6$ using atomic-resolution scanning transmission electron microscopy (STEM). Visualised for the *first time*, the local atomic structure reveals a unique and aperiodic stacking sequence in the layered mixed alkali ion compound. Moreover, we illustrate the potential of complex structures with intermixed alkali ions through electrochemistry and the conceptual demonstration of a dual cation battery using $NaKNi_2TeO_6$ as the cathode material that ideally matches both Na and K as the anode.

RESULTS

Mixed-alkali ion honeycomb layered oxides adopting the composition of $Na_{2-x}K_xNi_2TeO_6$ ($0 \leq x \leq 2$) were synthesised via a high-temperature solid-state synthesis route described in the **METHODS** section. A preliminary characterisation of the average crystal structures of the as-synthesised (pristine) materials was carried out using powder X-ray diffraction (XRD) (as shown in **Figure 1b**). When the smaller Na atoms were replaced with larger K atoms (*viz*., increasing x from 0 to 2), a stepwise shift comprised of several diffraction peaks was observed. Particularly, two discrete shifts are seen as 00l peaks of the $Na_{2-x}K_xNi_2TeO_6$ as shown in **Figure 1c**. Since the diffraction angles of the 00l peaks are inversely proportional to the distance between adjacent transition metal slabs (hereafter referred to as the interlayer distance), each position corresponds to a phase with a different interlayer distance. Two of the phases have interlayer distances closely resembling the parent materials $Na_2Ni_2TeO_6$ and $K_2Ni_2TeO_6$, whilst the last phase has an intermediate interlayer distance, indicating the existence of both Na and K atoms in this phase.

In order to quantify and better illustrate how the lattice parameters of the phases present in $Na_{2-x}K_xNi_2TeO_6$ change with varying amounts of Na and K, profile fitting (Le Bail fit) of the XRD patterns was subsequently carried out. The average lattice parameters as deduced from the fit, are provided in the **Supplementary Information** (**Supplementary Figure S1**). $Na_{2-x}K_xNi_2TeO_6$ compositions where $0.2 \leq x \leq 1.8$ are treated as two-phase mixtures, since the 00l Bragg peaks split into two separate peaks in these samples (as shown in **Figure 1c**). When K content (x, in $Na_{2-x}K_xNi_2TeO_6$) is increased with $Na_2Ni_2TeO_6$ as the starting material, the relative intensity of the peaks corresponding to the $Na_2Ni_2TeO_6$ phase decrease in favour of the new intermediate phase. It should be noted that when an equimolar ratio of Na and K is reached (*i.e*., $NaKNi_2TeO_6$), the $Na_2Ni_2TeO_6$ peaks disappear and new peaks emerge (as shown in **Figure 1d**). With further increase in the K content, the relative intensities of the peaks corresponding to the intermediate phase decreases and some other peaks disappear accordingly until pure $K_2Ni_2TeO_6$ is attained.

To reiterate, amongst the $Na_{2-x}K_xNi_2TeO_6$ diffraction patterns, peaks previously not found in the parent materials were observed in the mixed alkali compound. As illustrated by **Figure 1d,** a peak located at lower diffraction angles emerges in the intermediate compositions despite being forbidden in the $P6_3/mcm$ hexagonal space group

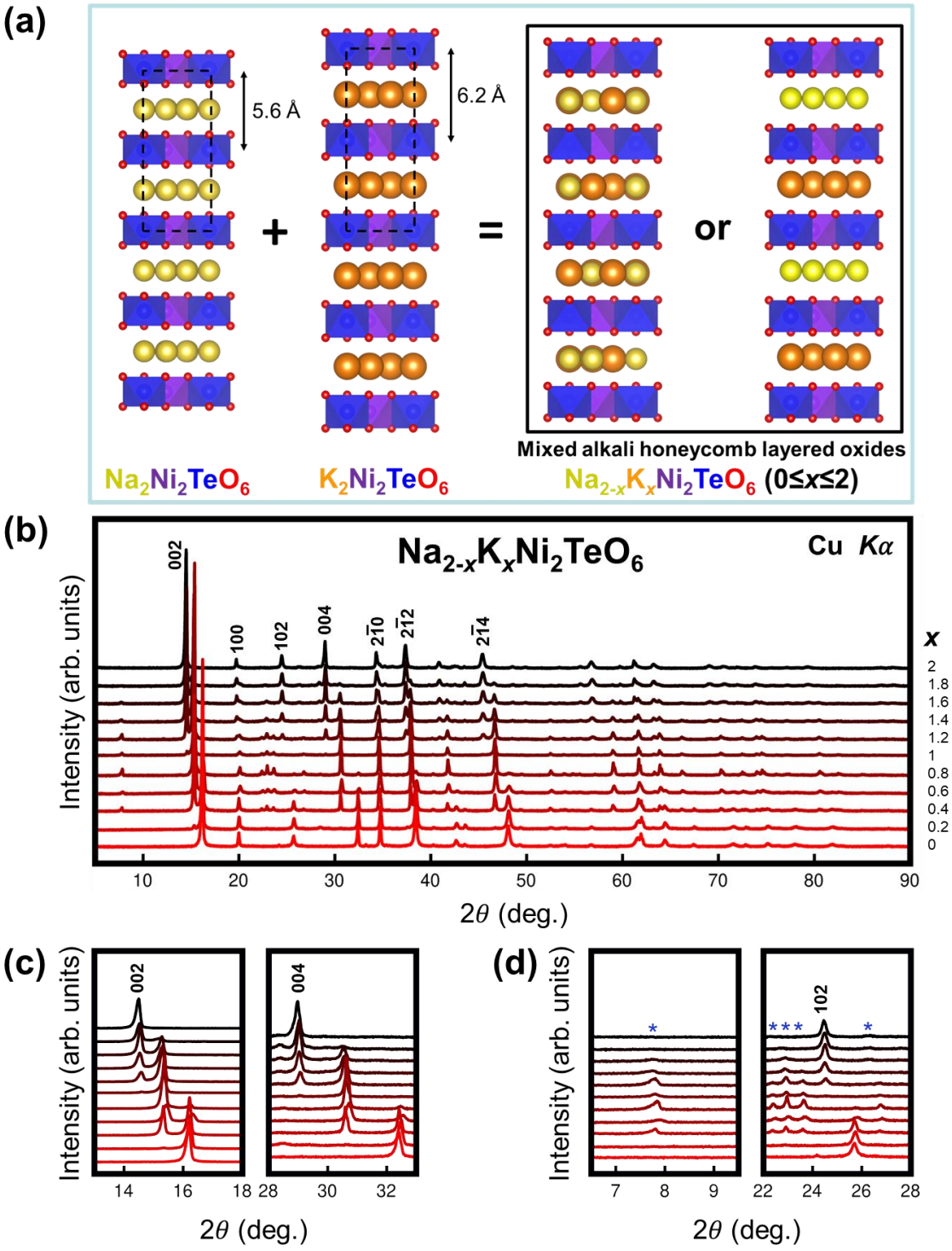

Figure 1. **X-ray diffraction (XRD) analyses of $Na_{2-x}K_xNi_2TeO_6$ ($0 \le x \le 2$).** **(a)** Schematic illustration of possible structural models in mixed alkali atom honeycomb layered oxides adopting the composition $Na_{2-x}K_xNi_2TeO_6$ ($0 \le x \le 2$). In the isostructural $A_2Ni_2TeO_6$ (A = Na, K) compounds, Na atoms (in yellow) or K atoms (in orange) are

sandwiched between layers or slabs consisting exclusively of TeO_6 (blue) and NiO_6 (purple) octahedra. Black dashed lines denote the unit cell. Owing to the larger Shannon-Prewitt ionic radius of K^+ (1.38 Å) compared to Na^+ (1.02 Å), the interlayer distance of $K_2Ni_2TeO_6$ is significantly larger than that of $Na_2Ni_2TeO_6$. Various reasonable structural models can be hypothesised for the new series of compounds adopting the composition $Na_{2-x}K_xNi_2TeO_6$ ($0 \leq x \leq 2$). Here, models where Na and K atoms are either mixed within the same layers or separated into different layers are shown. **(b)** XRD patterns of as-synthesised $Na_{2-x}K_xNi_2TeO_6$ ($0 \leq x \leq 2$), showing a stepwise shift of Bragg peaks towards lower diffraction angles with the substitution of Na with K. Bragg peaks for $K_2Ni_2TeO_6$ that are indexed in the hexagonal $P6_3/mcm$ space group are shown in black. Results of the elemental composition analyses of the prime intermediate compositions are furnished in the **Supplementary Information** (**Supplementary Table S1** and **Supplementary Figures S2**, **S3**, **S4**, **S5**, **S6**, **S7** and **S8**). **(c)** A stepwise shift of the 002 and 004 Bragg peaks that clearly hallmark the increase in the interlayer distance with K atom substitution. The three distinct peak positions correspond to three phases with different interlayer distances (along the *c*-axis), with the intermediate peak position signifying the formation of a new phase that is different from the end members $Na_2Ni_2TeO_6$ and $K_2Ni_2TeO_6$. **(d)** Emergence of new Bragg peaks in the intermediate compositions ($0 \leq x \leq 2$), which are not allowed in the $P6_3/mcm$ hexagonal space group. These new peaks are marked by asterisks and are indicative of a symmetry change that may entail the formation of superstructures.

used to index both $Na_2Ni_2TeO_6$ and $K_2Ni_2TeO_6$. Similar observations have been noted on a previous report on $Li_{3-x}Na_xNi_2SbO_6$ whereby disparate peaks emerged when Li and Na atoms were separated in different layers,[24] suggesting new cationic ordering in these new materials. As such, the disappearance of the 102 Bragg peak and the emergence of a new set of peaks in close proximity underline the structural changes occurring in this intermediate phase.

The tendency of these mixed-alkali ion compositions to separate into two-phase mixtures can be rationalised by the large difference in the Shannon-Prewitt ionic radii of Na^+ and K^+, [25] making it difficult to form a solid-solution compound from a mixture of $Na_2Ni_2TeO_6$ and $K_2Ni_2TeO_6$. Similar behaviour has also been observed amongst the layered nickelates $Na_xLi_{1-x}NiO_2$, where three different polymorphs with intermediate two-phase regions form depending on the stochiometric Li/Na ratio, presumably as a result of

the large difference between the ionic radii of Li and Na. [26] To further elucidate the manner of alkali atom arrangement upon successful intermixing of Na and K and the corresponding structural changes previously indicated by the XRD patterns (**Figure 1d**), crystal structural analyses were employed on $NaKNi_2TeO_6$ whose composition is closest to a phase-pure sample.

Synchrotron XRD measurements of $NaKNi_2TeO_6$ were performed for in-depth structural analyses, and its refinement result is shown in **Supplementary Figure S9**. We performed a Le Bail profile fitting using a hexagonal unit cell, yielding the lattice parameters of a = 5.2258(1) Å and c = 11.7875(6) Å and the reliability factors of R_{wp} = 8.96%, R_p = 6.27% and goodness-of-fit (GOF) = 4.12. We initially considered the reported structure of $Na_{1.97}Ni_2TeO_6$ in the $P6_3/mcm$ space group, [11] but disregarded this hexagonal space group because of the presence of the 001 and 003 reflections at ~3.01º and 9.05º. We also noticed that several peaks could not be fitted well with the initial structure considered. For example, the 100 and 003 reflections (**Supplementary Figure S9b**) were tailed and shifted towards higher angles, as previously observed in several layered oxides containing stacking faults (e.g., Li_2NiO_3 [59]). Preliminarily, we adopted several hexagonal models (some of which are shown in **Supplementary Figure S10**), in which Na and K are alternately arranged in a honeycomb layered framework. To ascertain information about the structure of $NaKNi_2TeO_6$, especially the stacking arrangement, atomic-resolution imaging of pristine $NaKNi_2TeO_6$ was conducted along several zone axes. Information on sample preparation, measurement protocols, and caveats undertaken are explicated in the **METHODS** section.

The atomic-resolution imaging was accomplished using an aberration-corrected scanning transmission electron microscopy (STEM). From the [001] zone axis, the characteristic honeycomb arrangement of transition metal atoms can be observed. **Figure 2a** shows a high-angle annular dark field (HAADF)-STEM image of the parent $K_2Ni_2TeO_6$. As the intensity is approximately proportional to the square of the atomic number (Z), [27–29] the honeycomb arrangement of heavier elements Te (Z = 52) and Ni (Z = 28) should be explicitly visualised through spots of varying intensities. This is evident in the analogous $K_2Ni_2TeO_6$ (see **Supplementary Figure S11**), where the red spots indicate columns of Ni atoms whilst the bright yellow spots correspond to columns of Te atoms. As such, it should be possible to acquire an analogous image for $NaKNi_2TeO_6$ if its honeycomb slab structure is similar to that of $K_2Ni_2TeO_6$. However, **Figure 2a** shows that all atomic sites

in the image share the same intensity, indicating "overlapping" of Ni and Te atoms in adjacent layers. It was also elusive to discern lighter (lower atomic mass) elements such as K and Na in the corresponding annular bright-field (ABF)-STEM images (shown in **Figure 2b**).

To clarify the structural changes responsible for the overlap of Ni and Te atoms observed in $NaKNi_2TeO_6$, the crystallites were examined from different directions (zone axes). A view from the [100] direction reveals the lamellar nature of the structure – in the HAADF-STEM image (**Figure 2c**), Te and Ni atoms correspond to a set of bright planes. This assignment was further confirmed by augmenting the STEM images with energy dispersive X-ray diffraction (EDX), as shown in **Supplementary Figure S12**. Elemental mapping using EDX also reveals that Na and K atoms are sandwiched between these Ni/Te-slabs. Furthermore, the STEM images reveal that Na and K are separated into different layers, instead of being randomly mixed within the same layers (**Figures 2d-f)**.

Further analyses of atomic-resolution STEM images from the [100] direction allow the stacking order in $NaKNi_2TeO_6$ to be characterised. Notably, the shift between adjacent Ni/Te slabs is contingent on whether the interlayer space is occupied by Na or K atoms (**Figure 2g**). No shift is observed when Ni/Te slabs are separated by a K layer. The alternating arrangement of Na and K atom layers was observed also when viewed along the $[1\bar{1}0]$ zone axis, as shown in **Supplementary Figure S13**. Moreover, the transition metal slabs sandwiching Na atoms are shifted by a period of 1/3 along or parallel to adjacent slabs. This stacking shift explains the observation of Ni and Te spots with approximately equal intensity when observed from the [001] direction (**Figures 2a** and **2b**), presumably owing to their overlapping. The direction of the slab shifts seems to be random lacking any periodicity, which explains the difficulties encountered in the structural and profile analyses of the powder diffraction patterns.

Attempts to determine whether the structure is truly random or aperiodic, albeit ordered to some degree, proved elusive. From an enlarged view of the atomic-scale HAADF-STEM mapping (**Figure 2h**), it is also evident that the interlayer distance depends on the alkali atom species sandwiched between adjacent Ni/Te layers. The Ni/Te layers with Na atoms are separated by 0.55 nm (5.5 Å) whilst the interlayer distance for the layers with K is 0.62 nm (6.2 Å). It is worth highlighting that these interlayer distances

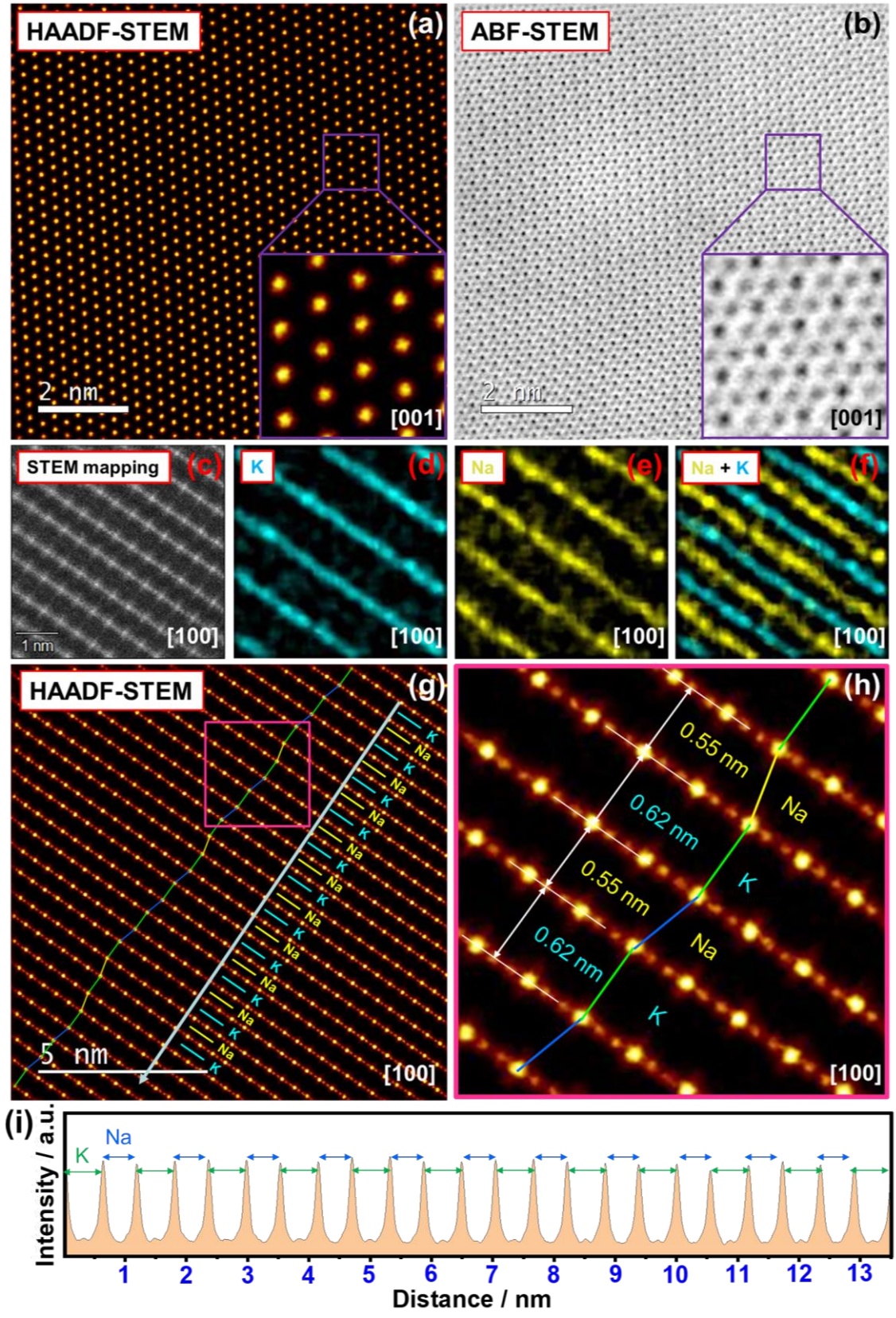

Figure 2. Arrangement of atoms in $NaKNi_2TeO_6$, viewed along the [001] and [100]

directions. **(a)** High-angle annular dark-field (HAADF) scanning transmission electron microscopy (STEM) images taken along the [001] zone axis. Overlap of Te and Ni atom positions in the adjacent layers along the *c*-axis result in spots with uniform intensity (when viewed in the [001] zone axis). **(b)** Corresponding annular bright-field (ABF)-STEM image, where also lighter elements (Na, K and O) can be visualised. **(c)** HAADF-STEM image of $NaKNi_2TeO_6$ taken along the [100] zone axis, revealing bright planes corresponding to the layers comprising Te and Ni, as further explicated in the corresponding energy dispersive X-ray (EDX) imaging (see **Supplementary Information** (**Supplementary Figure S12**) section). **(d, e and f)** STEM-EDX mapping of the area shown in **(a)**, where the colours explicitly visualise the distribution of Na and K atoms. The EDX maps show that the layers occupied by Na alternate with those of K. **(g)** HAADF-STEM image illustrating the unique stacking sequence in $NaKNi_2TeO_6$. In the layers where K atoms occupy the interlayer space, Te / Ni slabs are not shifted with respect to each other (marked by a green line). However, for layers where Na atoms reside, ±1/3 shifts of the Te / Ni slabs are observed. The yellow and blue lines show shifts in different directions. Note the aperiodicity in the stacking sequence. **(h)** Enlarged view of the domain highlighted in **(e)**, showing that the interlayer distance is contingent upon the alkali atom species (Na or K) sandwiched between the Te / Ni layers. **(i)** Line profile showing alternating interlayer distances occupied by K and Na, as shown by an arrow line in **(g)**.

attained closely resemble those of the parent compounds $Na_2Ni_2TeO_6$ and $K_2Ni_2TeO_6$ (**Figure 1a**). The intensity line profiles (shown in **Figure 2i**) quantitatively illustrate the alternating interlayer distances of Na and K atoms. Exclusively relying on the XRD patterns only yields the average of these interlayer spacings/distances (**Supplementary Figure S1**), accentuating the efficacy of using TEM to obtain important structural information.

Although the atomic structure of $NaKNi_2TeO_6$ exhibits significant aperiodicity, a partial structural model containing the slab shift can still be constructed based on the TEM analysis. **Figure 3a** illustrates an atomistic model viewed from the [100] direction, where the atomic coordinates based on $K_2Ni_2TeO_6$ structure obtained from XRD analysis were used. This model can be superimposed on both HAADF-STEM and ABF-STEM images, to confirm the accuracy of the positions of both heavier and lighter elements (**Figures 3b-c**). Comparison between the average structure model and the kinematically simulated selected area electron diffraction (SAED) pattern further supports the validity of the

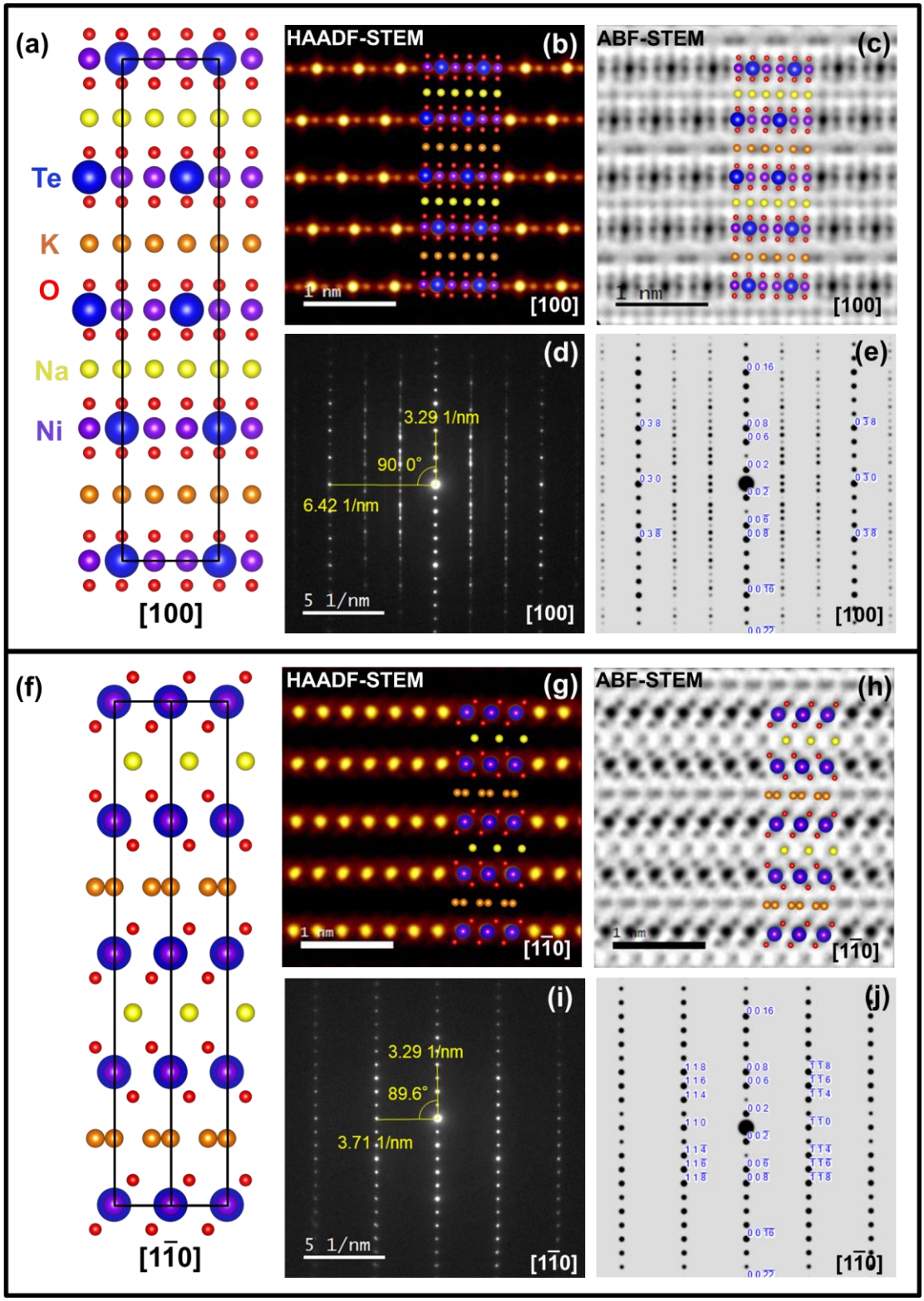

Figure 3. **Aperiodic atomic structure of $NaKNi_2TeO_6$ along the [100] and the [1$\bar{1}$0] zone axes.** **(a)** Atomistic model of the average aperiodic structure of $NaKNi_2TeO_6$ acquired based on STEM analyses along the [100] zone axis. Black lines show the partial

unit cell. **(b)** Superimposition of the model on a HAADF-STEM image, showing an excellent overlap between the positions of the Ni and Te atoms in the model that is in accord with the intensity distribution of the atom spots observed in the image. **(c)** Superimposition of the model on an annular dark-field (ADF) image, affirming the atomic positions of Na, K and O. **(d)** Selected area electron diffraction (SAED) patterns taken along the [100] zone axis revealing spot shifts and streaks that are suggestive of the existence of aperiodicity. **(e)** Corresponding kinematic simulations based on the structural model shown in **(a)**, showing agreement with the experimental results in **(d)**. **(f)** Atomistic model of $NaKNi_2TeO_6$ acquired based on STEM analyses along the $[1\bar{1}0]$ zone axis. Black lines show the partial unit cell. Note the difference in the arrangement of atoms between Na (yellow) and K (orange) crystallographic sites. **(g)** Superimposition of the model on a HAADF-STEM image, affirming the atomic positions of Ni and Te. **(h)** Superimposition of the model on an ABF-STEM image, also showing an excellent overlap between the positions of the Na, K and O atoms in the model that is in accord with the intensity distribution of the atom spots observed in the image. **(i)** SAED patterns taken along the $[1\bar{1}0]$ zone axis and **(j)** the corresponding kinematic simulations, validating good agreement with the experimental results shown in **(d)**.

obtained model (**Figures 3d-e**). The overall appearance of the simulation based on our model seems similar to the ones observed in the experiment, indicating that this partial model represents the average structure relatively well. However, the deviation of the peaks from the periodic arrangement and the presence of streaks along the [001] direction in the experimental SAED patterns (**Figure 3d**) attest to the aforementioned aperiodic stacking sequence.

To fully capture the atomistic model of $NaKNi_2TeO_6$, analyses along the $[1\bar{1}0]$ zone axes are complementary, as shown in the partial structure model (**Figure 3f**). Superimposing the model on both ABF-STEM and HAADF-STEM images yields excellent resemblance, thus confirming the accuracy of the alkali atom sites. In addition, the positions of Ni and Te atoms can be clearly distinguished in the HAADF-STEM image (**Figure 3g**). It should be noted that the shift of the metal slabs that was observed for all Na layers in the [100] direction was not observed in the $[1\bar{1}0]$ direction. Thus, the slab shift can be described as $[\pm 2/3 \ \pm 1/3 \ 0]$, corresponding to the swapping of Ni and Te site, which explains why Ni and Te sites were indistinguishable when observed in the [001] direction. Correspondingly, in the ABF-STEM superimposition, the Na and K atoms are seen as bright grey spots between the darker Te/Ni-atom planes (**Figure 3h**, showing a clear

difference between Na and K atom sites. The prismatic coordination of oxygen is clearly seen in the ABF-STEM images in both the Na and K layers. However, Na-atom sites are equidistantly spaced, whilst two adjacent K atom sites are grouped together.

Kinematically simulated SAED patterns in the $[1\bar{1}0]$ direction generated based on the model agree well with the experimentally determined diffraction pattern (**Figures. 3i-j**). No streaks nor peak deviations from periodic arrangement are observed in the diffraction pattern from the $[1\bar{1}0]$ zone axes (**Figure 3i**), as opposed to the [100] direction (**Figure 3d**). It validates that the $[1\bar{1}0]$ projected structure is completely periodic since the shift of Ni/Te layers possessing the aperiodicity occurs along this direction. In an attempt to reconcile the refinement results based on the synchrotron XRD data of $NaKNi_2TeO_6$, a comparison of the experimental SAED patterns with the structural model indexed in $P\bar{6}2c$ hexagonal space group was performed (**Supplementary Figure S14**), revealing $P\bar{6}2c$ hexagonal space group as appropriate to index the XRD pattern of $NaKNi_2TeO_6$. Rietveld refinement results of the synchrotron XRD and neutron diffraction patterns of $NaKNi_2TeO_6$ are furnished as **Supplementary Information** (**Supplementary Figures S15** and **S16**), with the refined parameters in **Supplementary Tables S2** and **S3**.

Structural intricacies of the mixed-alkali honeycomb layered oxide framework of $NaKNi_2TeO_6$ were further divulged by atomic-resolution STEM images (**Supplementary Figure S18**), which reveal the existence of stacking disorders/faults wherein ±1/3 shifts of the Te / Ni slabs are observed. To further quantitatively scrutinise the nature of the stacking faults innate in $NaKNi_2TeO_6$ as revealed by STEM (**Supplementary Figure S18**), the FAULTS program was employed.[54] The atomic structural model indexed in the $P\bar{6}2c$ hexagonal space group was used as the initial model to perform the analyses of the stacking faults. Various shift vectors were adopted to describe the stacking faults along the *c* plane, amongst which, shift vectors of [−1/3, −1/3, 0], [1/3, 0, 0] and [0, 1/3, 0] were found to be dominant with stacking probabilities of 7.5%, 6.3% and 4.1%, respectively. Taking all the results altogether, $NaKNi_2TeO_6$ possesses a high degree of stacking faults and we anticipate further study on the defect chemistry and physics of this class of honeycomb layered oxide materials in another scope of work.

DISCUSSION

A detailed characterisation of the crystal structure of a new mixed-alkali honeycomb layered oxide ($NaKNi_2TeO_6$) was achieved using aberration-corrected STEM. To our

knowledge, previous reports on the local atomic structure of a mixed-alkali ion layered oxide with similar structure have not been previously reported, making information on this class of materials obscure and underutilised. In the course of this study, a prominent aspect that emerges is the difference between Na and K sites evident when $NaKNi_2TeO_6$ crystals are viewed along the $[1\bar{1}0]$ and [100] zone axes. We find that, Na atoms are distributed in sites that assume triangular patterns (**Figure 4a**) whilst the K atoms reside in sites arranged in honeycomb formations (**Figure 4b**). Although beyond the limits of present experiments, these atomic configurations and crystallographic occupations can be used to predict emergent properties of such materials as well as the electrodynamics of the alkali or coinage atoms within the realm of their electromagnetic behaviour, electrochemistry, quantum phenomena *etc*. [30] For instance, the atomic arrangements of the atoms given in **Figure 4a** and **Figure 4b** are intricately linked to crystalline entropy considerations. This, in turn, can be envisaged to impact the electrodynamics of alkali ions in the material.

In particular, the free energy of the alkali atom layer is expected to be minimised (or equivalently, the entropy maximised) to achieve stability of the crystal especially when the Na or K atoms are arranged in a honeycomb fashion. This follows from the honeycomb conjecture, which states that the honeycomb lattice is the most efficient way of packing any two-dimensional (2D) surface with equal size unit cells of maximum area and minimum perimeter.[44] Thus, taking the free energy F to scale with the perimeter of the unit cells (honeycomb, triangular *etc.*), and the entropy to scale with the area, A, the lattice exhibited by K atoms in **Figure 4b** satisfies this conjecture by maintaining its honeycomb pattern whilst Na atoms in **Figure 4a** do not.

For the sake of rigour, we make a straightforward approximation for the free energy, F using the thermodynamics formula, $F = U - k_{\mathrm{B}}T\ln KA$, where K is a constant related to the geometry of the surface (Gaussian curvature),[30] $S = k_{\mathrm{B}}\ln KA$ is the entropy contribution to the free energy and $U \simeq -E_a$ is the internal potential energy corresponding to various binding energies of the alkali atoms (Na, K) to each other, whose leading term is taken to be their activation energy, E_a. Following this formula, the entire material comprising a series of such layers has to maximise entropy, even for the mixed alkali atom honeycomb layered oxides. As affirmed earlier, the highest entropy

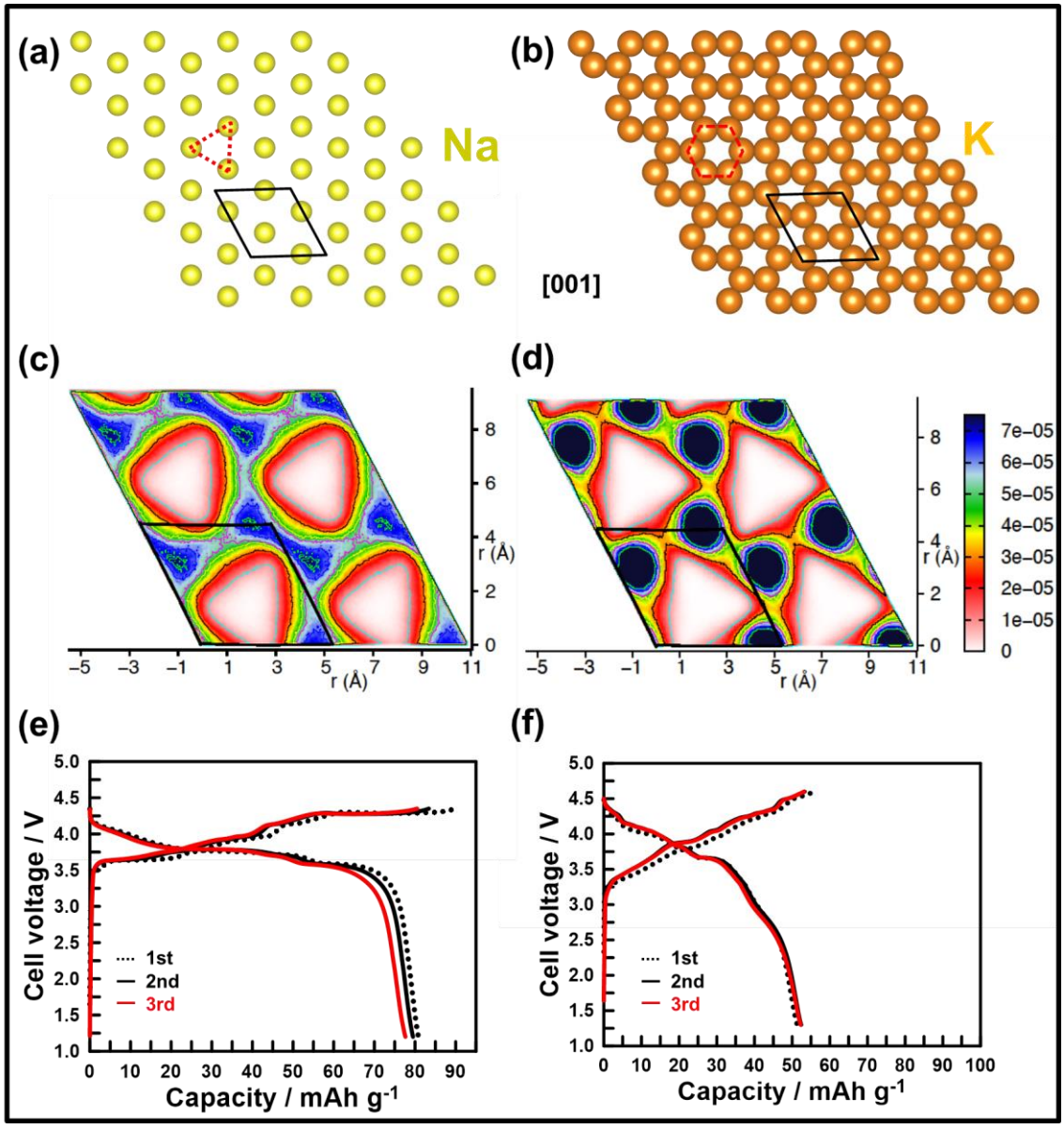

Figure 4. **Mixed alkali ion transport in $NaKNi_2TeO_6$.** **(a)** Arrangement of the Na atoms in triangular sites (as highlighted in red) as viewed along the [001] zone axis. The unit cell is highlighted in black lines. For clarity, the atoms denote the conformation of the sites and not the occupancy. **(b)** Honeycomb arrangement of K atoms in their respective sites as depicted along the [001] zone axis. **(c)** Molecular dynamics (MD) simulation showing the Na^+ ion probability density profile in the Na-layer (mapped onto 2 × 2 unit cells) using common colour bars (shown on the right). The population contours reflects that the preferred migration pathway amongst the interstitial cationic sites. **(d)** MD simulation for K^+ ion probability density profile in the K-layer. **(e)** Voltage-capacity profiles of $NaKNi_2TeO_6$ in Na-half cells using 1 M NaFSI in *N*-methyl-*N*-propylpyrrolidinium-based ($Pyrr_{13}FSI$) ionic liquid and **(f)** K-half cells using 1 M KFSI

in $Pyrr_{13}FSI$ ionic liquid. A current density of 6.65 mA g^{-1} commensurate to (dis)charging to a full theoretical two-electron capacity (C/20 rate) was used.

configuration leading to a minimised free energy and a stable crystalline structure is the one where both types of alkali atoms are arranged in a honeycomb fashion. The next favoured configuration is the one that allows for only one type of alkali atom to be in a honeycomb fashion, case in point being the configuration observed in $NaKNi_2TeO_6$ as displayed in **Figures 4a** and **4b**. Moreover, since the activation energy of K is lower than that of Na,[1,45] it is apparent, by setting $F = 0$, that the Na layer can still minimise its free energy by disrupting its honeycomb configuration into *e.g.* triangular patterns shown in **Figure 4a.** Thus, since the arrangement of the alkali atoms correlates with the adjacent metal slab atoms (Te, Ni), these slabs shear in order to accommodate the disruption, as observed in **Figure 2h**.

A similar entropic and free energy argument can be made to account for sodium and potassium spontaneously intercalating between the oxide layers separately albeit adjacent to each other. This corresponds to new binding energy terms in the potential energy inversely proportional to the separation distance of atoms of the same type. The simplest term can be written as $U(d) \simeq -E_a - \alpha/d^n$ where α is a positive constant, n a positive integer and d the separation distance of the atoms (*e.g.* for the binding energy offsetting the Coulomb repulsion between two alkali atoms of the same type, $\alpha = q^2/4\pi\epsilon$ is the fine structure constant and $n = 1$, where q is the charge of the adjacent alkali atom of the same type and ϵ is the permittivity across the distance, d). Thus, since a small separation distance, d further lowers the free energy of the material, the lowest stable free energy configuration is where $d = 0.62$ nm or $d = 0.55$ nm corresponding to the case of the pure atom $K_2Ni_2TeO_6$ or $Na_2Ni_2TeO_6$ respectively, where the distances are correlated with the ionic radii of the respective alkali atoms. Moreover, this strengthens the above argument for the disruption of the honeycomb pattern for Na in $NaKNi_2TeO_6$, since this new binding energy term is smaller for Na atoms compared to the case for K atoms, by virtue of a smaller d for Na atoms compared to K atoms. Finally, the next favoured configuration is given by, $d = (0.55 + 0.62)$nm, corresponding to the mixed alkali atom $NaKNi_2TeO_6$ reported herein, as shown in **Figure 2h**.

Molecular dynamics (MD) simulations can avail insights into the microscopic alkali-ion transport of functional materials. This information is useful to gauge the feasibility of $NaKNi_2TeO_6$ as an energy storage material. MD simulations were performed based on

the X-ray structure of $NaKNi_2TeO_6$, details of which are provided in the **METHODS** section. Computing the mean squared displacement at 600 K, we find that Na^+ ion has a higher diffusion coefficient (D) than K^+ ion based on the equation $\lim_{t\to\infty} < [\Delta r(t)]^2 > = 4Dt$, (where t is the time variable and $\Delta r(t)$ is the displacement of the cation) inside the conduction layer as is evident in **Supplementary Figure S19**. The Na^+ and K^+ ion population profile displayed in **Figures 4c** and **4d** also show the similar behavior within the structure of $NaKNi_2TeO_6$. A few high-density areas are identified in the population profile, indicating favourable sites of Na^+ or K^+ ions. Particularly, the high-density areas are well-connected for the Na-layer, whereas a modest connectivity amongst the high-density sites in K-layer is observed, resulting in higher diffusion of Na^+ ion compared to K^+ ion. It is worth to mention that this behaviour is different than the parent Na or K-systems *i.e.* $A_2Ni_2TeO_6$, where A = Na, K. This can be traced to the vastly different NiO_6 and TeO_6 octahedral stacking sequences from the parent Na or K-systems, which leads to a differing local environment.[1,44] Recall, we observed in STEM (**Figure 2g**) that, the layers where K atoms occupy the interlayer space, Te / Ni slabs are not shifted with respect to each other whereas, for layers where Na atoms reside, shifts of the Te / Ni slabs are observed. This behaviour is maintained in the simulation results despite high temperatures where the alkali ions are dynamic (see **Supplementary Video 1**). Further investigation of the nature of Na and K ion transport and its mechanism is beyond the scope of this work.

Presumably, $NaKNi_2TeO_6$ like other honeycomb layered oxides, holds potential in many fields. Nonetheless, the primary focus of this study is to ascertain its feasibility as a rechargeable battery electrode material. Thus, alkali-ion electrochemical tests were conducted to verify its capability to facilitate mixed-alkali ion extraction and insertion. Subsequently, separate Na and K half-cells were assembled, as further explicated in the **METHODS** section. Even though tellurium is not a constituent element of choice for energy storage systems entailing Earth-abundant elements, the insights obtained herein are not exclusive to the mixed-alkali tellurate systems. In essence, this study represents more of a scientific interest than a commercial one. Moreover, we do not rule out the use of tellurates in niche applications where functionality may be prioritised over cost. **Figure 4e** shows the voltage-capacity plots of $NaKNi_2TeO_6$ in Na half-cells. The theoretical capacity for a full Na^+ extraction from $NaKNi_2TeO_6$ is approximately 67 mAh g^{-1}. However, a reversible capacity of *ca.* 80 mAh g^{-1} was attained upon subsequent cycling, suggesting the occurrence of K^+ extraction. In the case of the K half-cells (**Figure**

4f), an initial capacity of 45 mAh g^{-1} was realised and maintained upon successive cycling. This capacity presumably arises from predominant K^+ extraction given that K metal was used.

High-resolution STEM imaging of electrodes subsequently cycled in Na- and K-half cells were performed, in order to ascertain the nature of the intercalation and de-intercalation process of the alkali-ions. **Figure 5a** shows the HAADF-STEM images of a $NaKNi_2TeO_6$ electrode upon subsequent cycling in Na-half cells taken at the [100] zone axis and the corresponding ABF-STEM images are shown in **Figure 5b**. SAED patterns taken along the [100] axis are shown in **Figure 5c**. Subsequent cycling of $NaKNi_2TeO_6$ in Na half-cells leads to the replacement of K^+ with Na^+ to yield a Na-rich phase composition ($Na_2Ni_2TeO_6$), as affirmed by the equidistant interlayer spacings (0.55 nm) of Na atoms along the [001] axis as quantitatively illustrated by the intensity line profiles (**Figure 5d**) for the highlighted area in the HAADF-STEM images (shown in **Figure 5a**). Streaks are evinced in the SAED patterns taken at the [100] axis (**Figure 5c**), indicating modulation in the arrangement of Na atoms along the *ab* plane as is exemplified in $Na_2Ni_2TeO_6$.[ref]

Figures 5e and **5f** show, respectively, the HAADF- and ABF-STEM micrographs of a $NaKNi_2TeO_6$ electrode upon cycling in K-half cells taken at [100] zone axis. **Figure 5g** shows the corresponding SAED patterns. Alternating interlayer spacings (0.55 nm and 0.62 nm) of Na and K atoms along the [001] axis is observed, indicating that the mixed alkali layered framework is retained owing to reversible extraction and insertion of K alone. Voltage-capacity plots of $NaKNi_2TeO_6$ upon subsequent cycling in K half-cells reveal a reversible initial capacity of approximately 50 mAh g^{-1} (**Figure 4f**). The theoretical capacity for a full K^+ extraction from $NaKNi_2TeO_6$ is approximately 67 mAh g^{-1}, which indicates that the capacity arises predominantly from K^+ extraction. Given that K metal was used as anode (counter electrode), reversible extraction and reinsertion of K can be envisaged, as is validated experimentally judging from the intensity line profile (**Figure 5h**) that quantitatively show alternating interlayer distances occupied by Na and K atoms. Further, SAED patterns (**Figure 5g**) show streaks indicative of the aperiodic stacking nature along the *c*-axis.

These electrochemical measurements indicate that $NaKNi_2TeO_6$ mixed-alkali honeycomb layered oxide is amenable to binary alkali-ion electrochemistry, pointing towards the possibility of developing a viable mixed Na- and K-ion electrochemical cell that relies on electrolytes and electrode materials that can accommodate both Na and K binary-cation

transport. Given that batteries utilising both cation and anion as charge carriers (dual-ion batteries (DIBs)) have already shown remarkable metrics in terms of energy density, power density and cycling life, [42,46–48] the present battery chemistry exploiting binary alkali metal cations could be a promising successor to DIB technology. By exploiting the

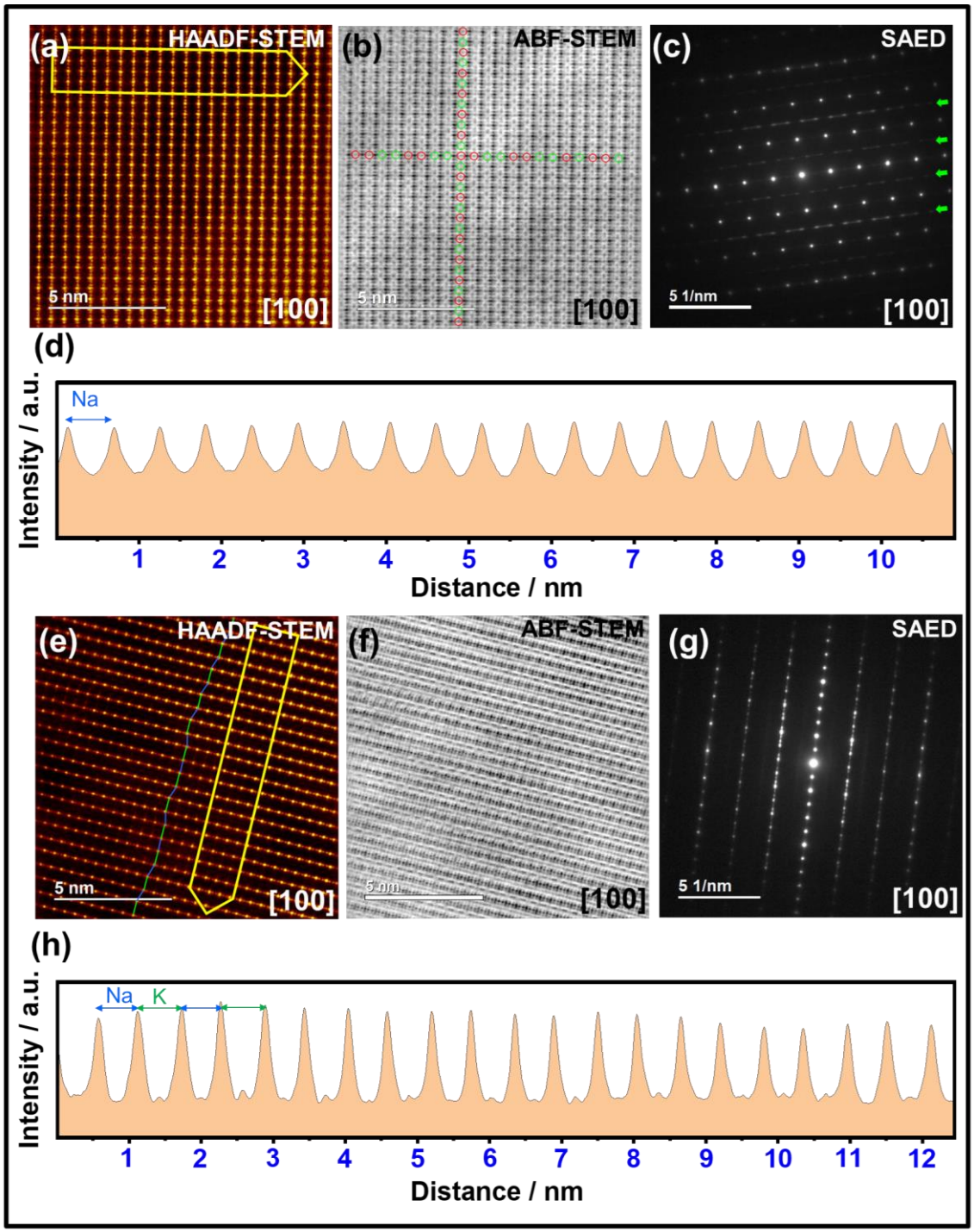

Figure 5. Structural changes during alkali-ion (de)insertion in $NaKNi_2TeO_6$. (a) HAADF-STEM images of $NaKNi_2TeO_6$ taken along the [100] axis upon cycling in a Na

half-cell. **(b)** Corresponding ABF-STEM images and **(c)** SAED patterns showing streaks (shown in green arrows) indicative of the modulation in the Na arrangement along the *ab* plane as is exemplified in $Na_2Ni_2TeO_6$. **(d)** Intensity line profiles as highlighted in (a) showing equidistant interlayer spacings (0.55 nm) of Na atoms along the [001] axis. **(e)** HAADF-STEM images of $NaKNi_2TeO_6$ taken along the [100] axis upon cycling in a K half-cell. **(f)** Corresponding ABF-STEM images and **(g)** SAED patterns showing streaks indicative of the aperiodic stacking nature along the *c*-axis. **(h)** Intensity line profiles as highlighted in **(e)** showing alternating interlayer spacings (0.55 nm and 0.62 nm) of Na and K atoms, respectively, along the [001] axis. For clarity, the horizontal axes in **(d)** and **(h)** show the number of layers. Intensity line profiles that quantitatively illustrate the interlayer spacing values shown in **(d)** and **(h)** are provided as **Supplementary Information** (**Supplementary Figures S20** and **S21**).

synergistic effect of Na- and K-ion electrochemistry, the battery confers the aforementioned metrics besides taking advantage of the abundance of Na and K resources. Moreover, it offers the possibility of utilising a NaK liquid metal alloy as anode material which is very effective in accommodating the cations, thwarting the formation of dendrites that have long plagued the direct utilisation of alkali metal anodes in secondary batteries (as succinctly demonstrated in **Figure 6a**).[60,61] Voltage-capacity plots of $NaKNi_2TeO_6$ when initially cycled in a NaK half-cell, using a mixed electrolyte based on a 0.5 M NaFSI + 0.5 M KFSI in $Pyr_{13}FSI$ ionic liquid, displays a reversible capacity of about 80 mAh g^{-1} at an average voltage of approximately 3.8 V (**Figure 6b**). The theoretical capacity of $NaKNi_2TeO_6$ is 134 mAh g^{-1}, assuming a full extraction of Na^+ and K^+ in a NaK cell. Although about 60% of theoretical capacity is attained, the performance is promising considering no electrode optimisation (carbon-coating, nanosizing, *etc*.) has been undertaken. The corresponding voltage-capacity plots at various current densities are shown in **Figure 6c**, indicating $NaKNi_2TeO_6$ sustains decent rate capabilities. Moreover, reversible electrochemical behaviour is observed with successive cycling as shown in **Figure 6d**. To fully tap the potential of $NaKNi_2TeO_6$, further electrode optimisation strategies are warranted, which is a subject of future work. **Figure 6e** shows voltage-capacity comparison plots of $NaKNi_2TeO_6$ along with cathode materials reported for NaK battery system. $NaKNi_2TeO_6$ is the first material to have both Na and K initially stabilised in its layered framework and offers a high voltage along with relatively high capacity. X-ray photoelectron spectroscopy measurements (shown in **Supplementary Figure S22**) indicate the participation of Ni to the charge compensation process, whereas Te is dormant, as has been noted in related honeycomb layered oxides

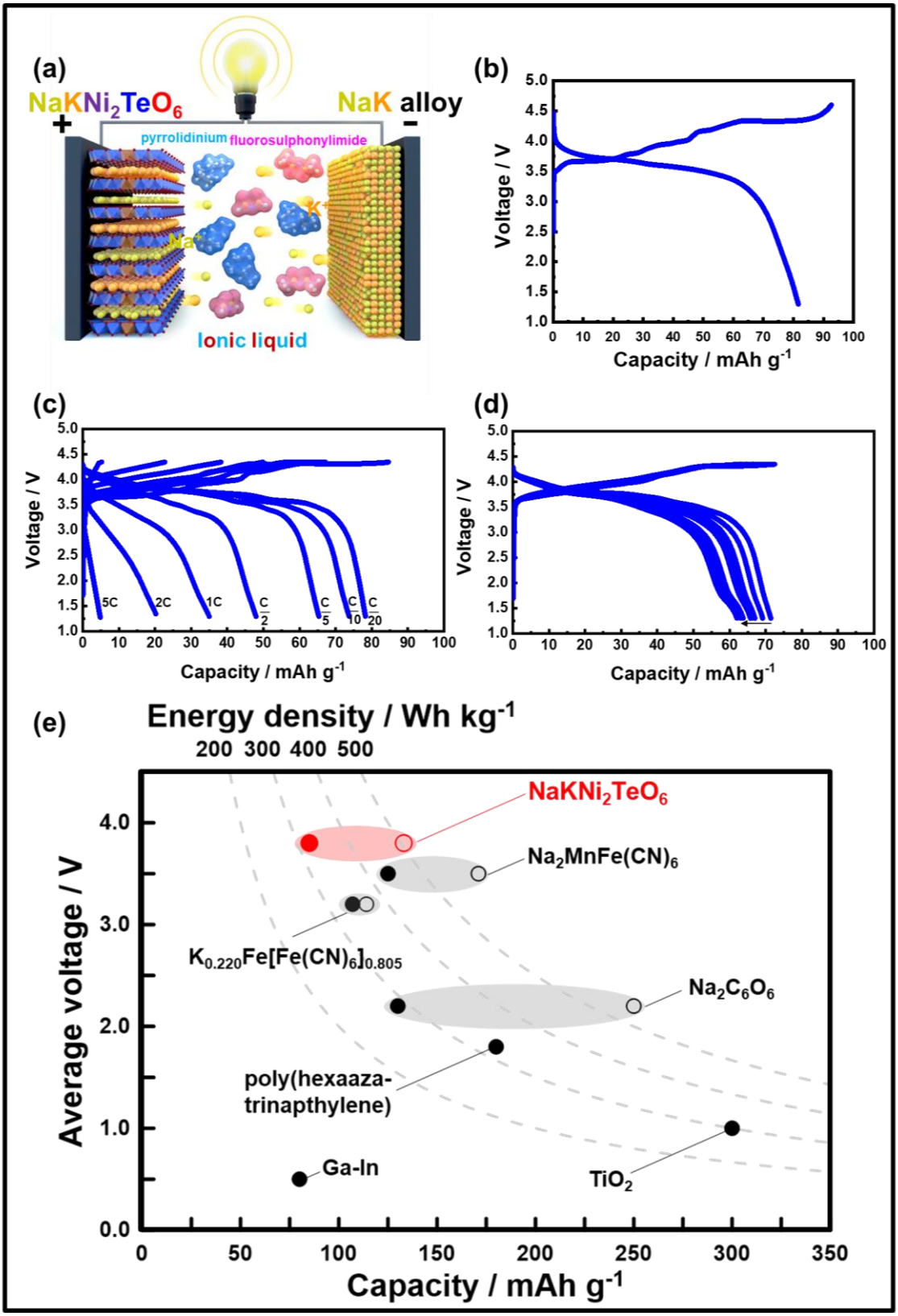

Figure 6. Electrochemical performance of $NaKNi_2TeO_6$ as a cathode material for NaK batteries. **(a)** A schematic illustration of a dual (Na- and K-ion) battery using

$NaKNi_2TeO_6$ as cathode and dendrite-free NaK liquid alloy as anode. **(b)** Voltage-capacity profiles of $NaKNi_2TeO_6$ dual-cation cathode material in a cell using NaK as anode during initial cycling. The electrolyte used was a 0.5 M NaFSI + 0.5 M KFSI in $Pyrr_{13}FSI$ dual-metal-cation ionic liquid. Details regarding the cell assembly are provided in the **METHODS** section. **(c)** Voltage-capacity profiles at various current densities commensurate to C/20, C/10, C/5, C/2, 1C, 2C and 5C rate. Here, 1C is commensurate to a current density of 134 mA g^{-1}. **(d)** Cyclability performance at a C/10 rate upon subsequent cycling (20 cycles). **(e)** Voltage-capacity plots of cathode materials reported so far for NaK batteries. Not only is $NaKNi_2TeO_6$ the first of its kind possessing both Na and K atoms, but also displays high voltages as a cathode material for NaK batteries. The electrochemical results not only highlight the practicality of a dual Na^+/K^+ cation battery but also the possibility of developing a 'dendrite-free' battery. Comparison data of $NaKNi_2TeO_6$ with reported cathode materials for NaK batteries is furnished as **Supplementary Table S4**.

such as $K_2Ni_2TeO_6$ and Na_4NiTeO_6.[2,4] With a judicious choice of constituent elements, we anticipate related mixed alkali compositions to exhibit even higher voltage and capacity.

Since both Na and K reinsertion can be envisaged during cycling of $NaKNi_2TeO_6$ in NaK cells, further structural insights were attained from high-resolution STEM measurements. **Figures 7a** and **7b** show the HAADF-STEM images along the [100] and $[1\bar{1}0]$ zone axes, respectively, for a $NaKNi_2TeO_6$ crystallite taken after subsequent cycling in NaK cell. Equidistant interlayer spacings are apparent, suggesting that one type of alkali-ion is reversibly reinserted into $NaKNi_2TeO_6$ upon successive cycling. Intensity line profiles reveal equidistant interlayer spacings (0.55 nm) corresponding to Na atoms in the lattice (**Figure 7c** and **Supplementary Figure S23**). Further, SAED patterns taken along the [100] and $[1\bar{1}0]$ zone axes (**Figures 7d** and **7e**) evidence streaks reminiscent of the modulation in the Na arrangement in Na-rich phase ($Na_2Ni_2TeO_6$).[57] Whilst only Na-rich phases are observed in TEM measurements, *ex situ* XRD measurements of discharged electrodes (**Supplementary Figure S24**) reveal K-rich and mixed alkali phases with Na-rich phase being predominant. These results reveal that there is a propensity of $NaKNi_2TeO_6$ to predominantly reinsert Na ions when cycled in NaK cells. Presumably, this could be rooted in the stability of $Na_2Ni_2TeO_6$ over other phases, as affirmed by theoretical computations (**Supplementary Figures S25**, **S26** and **S27**) that show the stability of Na-rich $Na_2Ni_2TeO_6$ over other phases such as $NaKNi_2TeO_6$ and $K_2Ni_2TeO_6$.

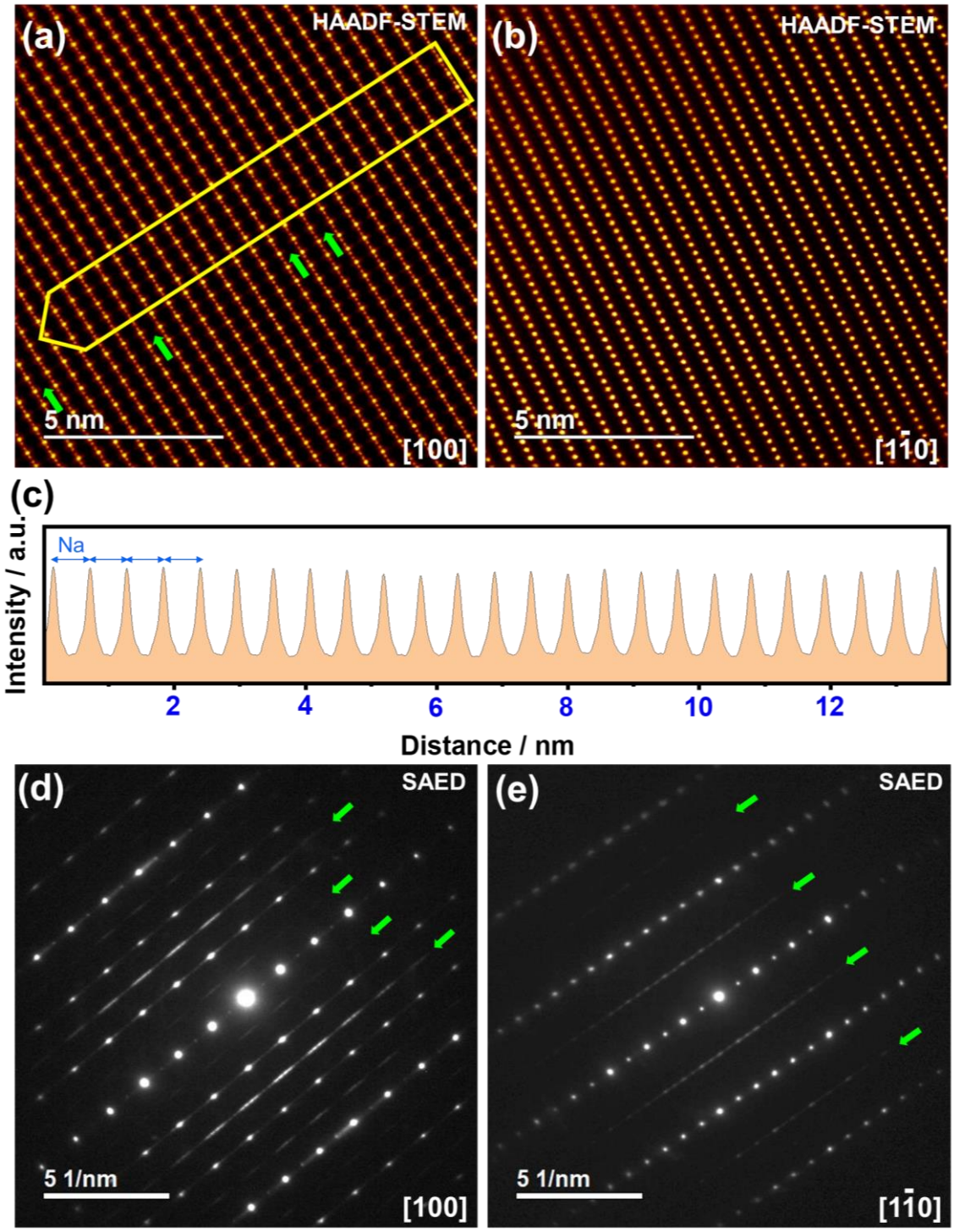

Figure 7. Structural changes during cycling of $NaKNi_2TeO_6$ in NaK batteries. HAADF-STEM images of $NaKNi_2TeO_6$ upon cycling in NaK battery cell taken along **(a)** [100] axis and **(b)** [1$\bar{1}$0] zone axis. Green arrows show Na atom layers where the adjacent Te/Ni slabs shift. A rationale for the slab shear transformations has been provided as **Supplementary Note 1**. **(c)** Intensity line profiles as highlighted in **(a)** showing

equidistant interlayer spacings (0.55 nm) along the [001] axis revealing $NaKNi_2TeO_6$ to preferentially insert Na atoms into the lattice. SAED patterns taken along **(d)** [100] axis and **(e)** $[1\bar{1}0]$ axis showing streaks (underpinned in green arrows) indicative of the modulation in the Na arrangement as is exemplified in $Na_2Ni_2TeO_6$.[57]

A close inspection of **Figure 7a** further reveals a variation in the Te/Ni stacking of the Na-rich phases, with domains where the slabs do not shift and domains where they do (highlighted by green arrows in **Figure 7a**) are observed. A rationale for the shear transformations has been appended as **Supplementary Note 1**.

It is imperative to mention that although the concept of mixed-alkali battery materials is not unprecedented, it has been found to ameliorate some battery functionalities. For instance, the substitution of Li atoms in layered transition metal cathode oxides with miniscule amounts of Na, K, Rb or Cs is a well-investigated route to enhance their structural stability and increase Li-ion diffusion. [31–39] However, the theoretical capacity of materials with similar amounts of different alkali metal atoms, such as $NaKNi_2TeO_6$, is drastically attenuated when large amounts of Na are replaced with K in a cathode for a Na-battery or *vice versa*. This is generally ascribed to the fact that the number of cations participating in extraction and reinsertion would be diminished. As a way to enhance performance, the utilisation of an alloy such as NaK in the case of $NaKNi_2TeO_6$ would facilitate the participation of both cation species thus yield high theoretical capacity, as demonstrated in **Figure 6a**. In addition, the liquid nature of NaK does not allow the formation of dendrite on the anode thus rendering the design 'a dendrite-free' metal anode battery. Therefore, this concept showcases the potential for $NaKNi_2TeO_6$ and related mixed-alkali layered oxide materials as functional materials.

Motivated by the projected functionalities of such materials, attempts were made to synthesise various compositions that form structures akin to those of $NaKNi_2TeO_6$. Partial substitution of Ni with Co, lead to the successful synthesis of mixed-alkali layered oxides adopting the compositions $Na_{2-x}K_xNi_{2-y}Co_yTeO_6$ (y = 0.25, 0.5, 0.75, 0.1) (as shown in **Supplementary Figures S28** and **S29**). Material characterisation using XRD data confirm the formation of intermediate phases regardless of the extent of Co-doping, highlighting the possibility to create structures similar to that of $NaKNi_2TeO_6$ in other compositions such as $NaKM_2TeO_6$ (M = Cu, Zn, Co) as shown in **Supplementary Figure S30.** In addition, this work has also accentuated the further exploration of other mixed

alkali honeycomb layered oxides that entail alkali atoms such as Li (as shown in **Supplementary Figure S31**).

In conclusion, the successful design of mixed-alkali honeycomb layered oxides, for instance $NaKNi_2TeO_6$, not only offers a conduit to engineering new functional materials but also promises to expand the compositional space of known honeycomb layered oxides. The results of this study reaffirm the correlation between the ionic radii of the alkali atoms and the interlayer distance even for the mixed-alkali system, which can be exploited to configure the intricate interlayer structure of the mixed-alkali honeycomb layered oxides, by the same token as $Ag/LiCoO_2$. [40] Detailed local atomic information provided through a series of scanning transmission electron microscopy (STEM) reveal characteristics of a unique aperiodic stacking structure, suggesting structural versatility that could unlock the potential of this material for fascinating electromagnetic, quantum and electrochemical functionalities. [1,30,41] Further, we expound on the feasibility of $NaKNi_2TeO_6$ for battery applications that utilise mixed cation transport. The mixed triangular and honeycomb atomics conformations may have profound impact on the electrodynamics of the alkali ions. An attempt to rationalise this view has been made by theoretical computations. We hope that this work will serve as a cornerstone for further augmentation of mixed-alkali layered oxides in various realms of science and technology.

References

1. Kanyolo, G. M. *et al*. Honeycomb Layered Oxides: Structure, Energy Storage, Transport, Topology and Relevant Insights. *Chem. Soc. Rev.* **50**, 3990–4030 (2021).
2. Masese, T. *et al*. Rechargeable potassium-ion batteries with honeycomb-layered tellurates as high voltage cathodes and fast potassium-ion conductors. *Nat. Commun*. **9**, 3823 (2018).
3. Masese, T. *et al*. A high voltage honeycomb layered cathode framework for rechargeable potassium-ion battery: P2-type $K_{2/3}Ni_{1/3}Co_{1/3}Te_{1/3}O_2$. *Chem. Commun*. **55**, 985–988 (2019).
4. Yang, Z. *et al*. A high-voltage honeycomb-layered Na_4NiTeO_6 as cathode material for Na-ion batteries. *J. Power Sources* **360**, 319–323 (2017).
5. Yuan, D. *et al*. A Honeycomb-Layered $Na_3Ni_2SbO_6$: A High-Rate and Cycle-Stable Cathode for Sodium-Ion Batteries. *Adv. Mater*. **26**, 6301–6306 (2014).
6. Sathiya, M. *et al*. Li_4NiTeO_6 as a positive electrode for Li-ion batteries. *Chem. Commun*. **49**, 11376–11378 (2013).

7. Bhange, D. S. *et al*. Honeycomb-layer structured $Na_3Ni_2BiO_6$ as a high voltage and long life cathode material for sodium-ion batteries. *J. Mater. Chem*. *A* **5**, 1300–1310 (2017).
8. Yoshii, K. *et al*. Sulfonylamide-Based Ionic Liquids for High-Voltage Potassium-Ion Batteries with Honeycomb Layered Cathode Oxides. *ChemElectroChem* **6**, 3901–3910 (2019).
9. Wang, P.-F. *et al*. An Ordered Ni_6-Ring Superstructure Enables a Highly Stable Sodium Oxide Cathode. *Adv. Mater*. **31**, 1903483 (2019).
10. Kitaev, A. Anyons in an exactly solved model and beyond. *Ann. Phys.* (N. Y). **321**, 2–111 (2006).
11. Evstigneeva, M. A., Nalbandyan, V. B., Petrenko, A. A., Medvedev, B. S. & Kataev, A. A. A new family of fast sodium ion conductors: $Na_2M_2TeO_6$ (*M* = Ni, Co, Zn, Mg). *Chem. Mater*. **23**, 1174–1181 (2011).
12. Nalbandyan, V. B., Petrenko, A. A. & Evstigneeva, M. A. Heterovalent substitutions in $Na_2M_2TeO_6$ family: Crystal structure, fast sodium ion conduction and phase transition of $Na_2LiFeTeO_6$. *Solid State Ionics* **233**, 7–11 (2013).
13. Kumar, V., Bhardwaj, N., Tomar, N., Thakral, V. & Uma, S. Novel Lithium-Containing Honeycomb Structures. *Inorg. Chem*. **51**, 10471–10473 (2012).
14. Li, Y. *et al*. New P2-Type Honeycomb-Layered Sodium-Ion Conductor: $Na_2Mg_2TeO_6$. *ACS Appl. Mater. Interfaces* **10**, 15760–15766 (2018).
15. Wu, J.-F., Wang, Q. & Guo, X. Sodium-ion conduction in $Na_2Zn_2TeO_6$ solid electrolytes. *J. Power Sources* **402**, 513–518 (2018).
16. Sau, K. & Kumar, P. P. Role of Ion–Ion Correlations on Fast Ion Transport: Molecular Dynamics Simulation of $Na_2Ni_2TeO_6$. *J. Phys. Chem. C* **119**, 18030–18037 (2015).
17. Sau, K. Influence of ion–ion correlation on Na^+ transport in $Na_2Ni_2TeO_6$: molecular dynamics study. *Ionics* (Kiel). **22**, 2379–2385 (2016).
18. Delmas, C., Fouassier, C., Réau, J.-M. & Hagenmuller, P. Sur de nouveaux conducteurs ioniques a structure lamellaire. *Mater. Res. Bull*. **11**, 1081–1086 (1976).
19. Balsys, R. J. & Lindsay Davis, R. The structure of $Li_{0.43}Na_{0.36}CoO_{1.96}$ using neutron powder diffraction. *Solid State Ionics* **69**, 69–74 (1994).
20. Berthelot, R., Pollet, M., Carlier, D. & Delmas, C. Reinvestigation of the OP4-(Li/Na)CoO_2-layered system and first evidence of the (Li/Na/Na)CoO_2 phase with OPP9 oxygen stacking. *Inorg. Chem.* **50**, 2420–2430 (2011).
21. Ren, Z. *et al*. Enhanced thermopower in an intergrowth cobalt oxide $Li_{0.48}Na_{0.35}CoO_2$. *J. Phys. Condens. Matter* **18**, L379–L384 (2006).

22. Yabuuchi, N. *et al*. A Comparative Study of $LiCoO_2$ Polymorphs: Structural and Electrochemical Characterization of O2-, O3-, and O4-type Phases. *Inorg. Chem*. **52**, 9131−9142 (2013).

23. Komaba, S., Yabuuchi, N. & Kawamoto, Y. A New Polymorph of Layered $LiCoO_2$. *Chem. Lett.* **38**, 954–955 (2009).

24. Vallée, C. *et al*. Alkali-Glass Behavior in Honeycomb-Type Layered $Li_{3-x}Na_xNi_2SbO_6$ Solid Solution. *Inorg. Chem.* **58**, 11546–11552 (2019).

25. Shannon, R. D. Revised effective ionic radii and systematic studies of interatomic distances in halides and chalcogenides. *Acta Crystallogr. Sect. A* **32**, 751–767 (1976).

26. Holzapfel, M. *et al*. Mixed layered oxide phases $Na_xLi_{1-x}NiO_2$: A detailed description of their preparation and structural and magnetic identification. *Solid State Sci.* **7**, 497–506 (2005).

27. Pennycook, S. J. *et al*. Scanning Transmission Electron Microscopy for Nanostructure Characterization. in Scanning Microscopy for Nanotechnology: Techniques and Applications (eds. Zhou, W. & Wang, Z. L.) 152–191 (Springer, 2006).

28. Pennycook, S. J. & Boatner, L. A. Chemically sensitive structure-imaging with a scanning transmission electron microscope. *Nature* **336**, 565–567 (1988).

29. Pennycook, S. J., Varela, M., Hetherington, C. J. D. & Kirkland, A. I. Materials Advances through Aberration-Corrected Electron Microscopy. *MRS Bull*. **31**, 36–43 (2006).

30. Kanyolo, G. M. & Masese, T. An Idealised Approach of Geometry and Topology to the Diffusion of Cations in Honeycomb Layered Oxide Frameworks. *Sci. Rep.* **10**, 13284 (2020).

31. Li, Q. *et al*. K^+-doped $Li_{1.2}Mn_{0.54}Co_{0.13}Ni_{0.13}O_2$: A novel cathode material with an enhanced cycling stability for lithium-ion batteries. *ACS Appl. Mater. Interfaces* **6**, 10330–10341 (2014).

32. He, W. *et al.* Enhanced high-rate capability and cycling stability of Na-stabilized layered $Li_{1.2}[Co_{0.13}Ni_{0.13}Mn_{0.54}]O_2$ cathode material. *J. Mater. Chem. A* **1**, 11397–11403 (2013).

33. Li, N. *et al.* Incorporation of rubidium cations into $Li_{1.2}Mn_{0.54}Co_{0.13}Ni_{0.13}O_2$ layered oxide cathodes for improved cycling stability. *Electrochim. Acta* **231**, 363–370 (2017).

34. Zheng, J. *et al*. Li- and Mn-Rich Cathode Materials: Challenges to Commercialization. *Adv. Energy Mater.* **7**, (2017).

35. Dahiya, P. P., Ghanty, C., Sahoo, K., Basu, S. & Majumder, S. B. Effect of

Potassium Doping on the Electrochemical Properties of $0.5Li_2MnO_3$-$0.5LiMn_{0.375}Ni_{0.375}Co_{0.25}O_2$ Cathode. *J. Electrochem. Soc.* **165**, A2536–A2548 (2018).

36. Ding, X. *et al.* Cesium doping to improve the electrochemical performance of layered $Li_{1.2}Ni_{0.13}Co_{0.13}Mn_{0.54}O_2$ cathode material. *J. Alloys Compd.* **791**, 100–108 (2019).

37. Ates, M. N. *et al*. Mitigation of Layered to Spinel Conversion of a Li-Rich Layered Metal Oxide Cathode Material for Li-Ion Batteries. *J. Electrochem. Soc.* **161**, A290–A301 (2014).

38. Guan, L., Xiao, P., Lv, T., Zhang, D. & Chang, C. Improved Electrochemical Performance of $Rb_xLi_{1.27-x}Cr_{0.2}Mn_{0.53}O_2$ Cathode Materials via Incorporation of Rubidium Cations into the Original Li Sites. *J. Electrochem. Soc.* **164**, A3310–A3318 (2017).

39. Dong, J., Xiao, P., Zhang, D. & Chang, C. Enhanced rate performance and cycle stability of $LiNi_{0.8}Co_{0.15}Al_{0.05}O_2$ via Rb doping. *J. Mater. Sci. Mater. Electron.* **29**, 21119–21129 (2018).

40. Berthelot, R., Pollet, M., Doumerc, J. & Delmas, C. $(Li/Ag)CoO_2$: A New Intergrowth Cobalt Oxide Composed of Rock Salt and Delafossite Layers. *Inorg. Chem.* **50**, 6649–6655 (2011).

41. Zhang, H., Arlego, M. & Lamas, C. A. Quantum phases in the frustrated Heisenberg model on the bilayer honeycomb lattice. *Phys. Rev. B* **89**, 024403 (2014).

42. Wang, M. & Tang, Y. B. A Review on the Features and Progress of Dual-Ion Batteries. *Adv. Mater.* **8**, 1703320 (2018).

43. Petříček, V., Dušek, M. & Palatinus, L. Crystallographic Computing System JANA2006: General features. *Z. Kristallogr. Cryst. Mater.* **229**, 345–352 (2014).

44. Matsubara, N. *et al*. Magnetism and Ion Diffusion in Honeycomb Layered Oxide $K_2Ni_2TeO_6$: First Time Study by Muon Spin Rotation & Neutron Scattering. *Sci. Rep.* **10**, 18305 (2020).

45. Xue, L., Gao, H., Li, Y. & Goodenough, J. B. Cathode Dependence of Liquid-Alloy Na–K Anodes. *J. Am. Chem. Soc.* **140**, 3292–3298 (2018).

46. Guo, X., Zhang, L., Ding, Y., Goodenough, J. B. & Yu, G. Room-temperature liquid metal and alloy systems for energy storage applications. *Energy Environ. Sci. Soc.* **12**, 2605–2619 (2019).

47. Chen, C. –Y., Matsumoto, K., Kubota, K., Hagiwara, R. & Xu, Q. An Energy‐Dense Solvent‐Free Dual‐Ion Battery. *Adv. Funct. Mater.,* https://doi.org/10.1002/adfm.202003557 (2020).

48. Matsumoto, K., Okamoto, Y., Nohira, T. & Hagiwara, R. Thermal and Transport Properties of $Na[N(SO_2F)_2]$–[*N*-Methyl-*N*-propylpyrrolidinium]$[N(SO_2F)_2]$ Ionic

Liquids for Na Secondary Batteries. *J. Phys. Chem. C* **119**, 7648–7655 (2015).
49. Matsumoto, K., Hwang, J., Kaushik, S., Chen, C. –Y. & Hagiwara, R. Advances in sodium secondary batteries utilizing ionic liquid electrolytes. *Energy Environ. Sci.* **12**, 3247–3287 (2019).
50. Yamamoto, T., Matsumoto, K., Hagiwara, R. & Nohira, T. Physicochemical and Electrochemical Properties of K[N($SO_2F)_2$]–[*N*-Methyl-*N*-propylpyrrolidinium][N($SO_2F)_2$] Ionic Liquids for Potassium-Ion Batteries. *J. Phys. Chem. C* **121**, 18450–18458 (2017).
51. Saito, M., Kimoto, K., Nagai, T., Fukushima, S., Akahoshi, D., Kuwahara, H., Matsui, Y., & Ishizuka, K. Local crystal structure analysis with 10-pm accuracy using scanning transmission electron microscopy. *J. Electron Microsc.* **53** 131–136 (2009).
52. Sau, K. & Kumar, P. P. Ion Transport in $Na_2M_2TeO_6$: Insights from Molecular Dynamics Simulation. *J. Phys. Chem. C* **119** 1651–1658 (2015).
53. Plimpton, S. Fast parallel algorithms for short-range molecular dynamics. *J. Comp. Phys.* **117** 1–19 (1995).
54. Casas-Cabanas, M. *et al*. FAULTS: a program for refinement of structures with extended defects. *J. Appl. Cryst.* **49** 2259–2269 (2016).
55. Oishi-Tomiyasu, R. *et al*. Application of matrix decomposition algorithms for singular matrices to the Pawley method in Z-Rietveld. *J. Appl. Cryst.* **45** 299–308 (2012).
56. Perdew, J. P., Burke, K. & Ernzerhof, M. Generalized gradient approximation made simple. *Phys. Rev. Lett.* **77**, 3865–3868 (1996).
57. Masese, T. *et al*. Unveiling structural disorders in honeycomb layered oxide: $Na_2Ni_2TeO_6$. *Materialia* **15**, 101003 (2021).
58. Momma, K. & Izumi, F. VESTA 3 for three-dimensional visualization of crystal, volumetric and morphology data. *J. Appl. Crystallogr.* 44, 1272–1276 (2011).
59. Bianchini, M. *et al*. From $LiNiO_2$ to Li_2NiO_3: Synthesis, Structures and Electrochemical Mechanisms in Li-Rich Nickel Oxides. *Chem. Mater.* **32**, 9211–9227 (2020).
60. Xue, L. *et al*. Liquid K‐Na Alloy Anode Enables Dendrite‐Free Potassium Batteries. *Adv. Mater.* **28**, 9608–9612 (2016).
61. Huang, M. *et al*. New Insights into the Electrochemistry Superiority of Liquid Na–K Alloy in Metal Batteries. *Small* **15**, 1804916 (2019).

Acknowledgements

We thank Ms. Shinobu Wada and Mr. Hiroshi Kimura for the unrelenting support in undertaking this study. We gratefully acknowledge Ms. Kumi Shiokawa, Mr. Masahiro Hirata and Ms. Machiko Kakiuchi for their advice and technical help as we conducted the syntheses, electrochemical and XRD measurements. This work was supported by the TEPCO Memorial Foundation. In addition, this work was also conducted in part under the auspices of the Japan Society for the Promotion of Science (JSPS KAKENHI Grant Number 19K15685), Sumika Chemical Analyses Services (SCAS) Co. Ltd., National Institute of Advanced Industrial Science and Technology (AIST) and Japan Prize Foundation. We thank Dr. T. Saito for the assistance in the neutron diffraction experiments. The neutron diffraction measurements at J-PARC were performed with the approval of the proposal numbers 2017L1302 and 2020L0802. This study was partly supported by Grants-in-Aid for Scientific Research (KAKENHI, No. JP19H00821 and JP20K05086) from the Ministry of Education, Culture, Sports, Science and Technology of Japan. T. M. gratefully acknowledges Natsumi Ishii and Rei Ishii for the unwavering support in conducting this work.

Data availability

The data that support the findings of this study (Supplementary materials including experimental (methods) details) will be availed during the production stage.

Competing interests

The authors declare no competing interests.